Sensors and Materials, Vol. 38, No. 1 (2026) 27–54
MYU Tokyo

S & M 4282

High-precision Adaptive Photoelectric Encoder Using Triple Image Sensors in 120° Symmetric Layout

Yimang Li, Yijie Chen,* Tao Liu, and Wenxiu Zhang

Changzhou University, No. 21, Gehu Middle Road, Wujin District,
Changzhou City, Jiangsu Province, P.R. China

(Received September 5, 2025; accepted November 17, 2025)

Keywords: angular measurement precision, EKF, triple-sensor system, self-adaptive

The escalating demand for angular measurement precision in industrial automation and precision manufacturing has driven significant research into image-based photoelectric encoders, valued for their noncontact operation and high-resolution capabilities. In this study, we present a self-adaptive angular displacement measurement model utilizing triple image sensors to mitigate pronounced even-order harmonic errors and inadequate environmental susceptibility in conventional single/dual-sensor systems. The proposed design integrates a 120° symmetric configuration with a hybrid "mechanical calibration-algorithmic compensation-environmental adaptation" strategy, enhanced by extended Kalman filter (EKF) bias estimation and gradient descent weight optimization. Simulation and experimental results demonstrate that the triple-sensor system reduces the second harmonic component ratio from 2.1% (dual-sensor baseline) to 0.6%, achieving 71% harmonic suppression. Static repeatability improves by 65% (±1.2″ vs ±3.5″), while dynamic interpolation error decreases by 66% (±1.2″ vs ±3.5″). Environmental robustness tests reveal an 80% reduction in temperature drift coefficient (±0.5″/°C vs ±2.5″/°C) and an 8 dB enhancement in vibration noise rejection (50 dB vs 42 dB). The system maintains ±1.8″ accuracy under single-point failure. Through nanoimprinted gratings and 3D stacked packaging, a 40% reduction in system volume and a 30% lower power consumption are achieved, compared with conventional implementations. This work provides both theoretical and practical foundations for high-precision photoelectric encoder engineering.

1. Introduction

High-precision angular displacement metrology serves as a foundational technology for advanced manufacturing, aerospace systems, and robotic control. The global push for Industry 4.0 and intelligent manufacturing has intensified the demand for precision measurement systems. In computer numerical control (CNC) machining, for example, machining accuracy is directly contingent upon the angular displacement measurement precision of encoders.[1] Modern machine tools now require submicron positioning accuracy (<0.1 μm), necessitating angular resolutions of 0.01″. However, conventional photoelectric encoders face fundamental

*Corresponding author: e-mail: 374136445@qq.com
https://doi.org/10.18494/SAM5920

ISSN 0914-4935
https://myukk.org/

limitations owing to grating fabrication processes and Moiré fringe interpolation techniques, typically capping the resolution at 20–23 bits, which is insufficient for emerging applications. An image-based photoelectric encoder represents a breakthrough, enabling high-precision angular computation through direct acquisition via image sensors and computational algorithms. This approach theoretically achieves resolutions exceeding 26 bits. For instance, Heidenhain's (Germany) ERA4882C encoder, utilizing a single CMOS sensor, attains 25-bit resolution. However, its performance deteriorates in complex industrial environments owing to inherent single-sensor limitations, including poor noise immunity and significant even-order harmonic errors.

Current research on image-based photoelectric encoders predominantly focuses on single- and dual-sensor architectures. Single-sensor configurations, such as Nikon's LN-150 series (Japan),[(2)] deliver ±1″ static accuracy through interpolation algorithms. However, the lack of redundancy fails aerospace-grade reliability requirements. Dual-sensor systems, as studied by Changchun Institute of Optics,[(3)] demonstrate partial improvement through spatial symmetry, reducing interpolation errors to ±2.5″ via differential signal processing. This approach further comes at the cost of 40% increased power consumption and 30% larger package volume.[(4)] A quad-sensor encoder developed by Kim and Voyles[(5)] achieves single-point failure tolerance through redundant voting, yet requires ±0.1 μm assembly precision, exceeding current manufacturing capabilities. Based on the above references, current image-based photoelectric encoders exhibit three critical limitations: (i) notable deficiencies in environmental adaptability and prominent dynamic inaccuracies, (ii) insufficient reliability and redundancy, and (iii) an inherent trade-off between performance and system practicality.

To address the issue of varying numbers of sensors mentioned above, we present an adaptive angular displacement measurement system employing a triple image-sensor configuration. The developed solution establishes a harmonic suppression model based on a 120° symmetric arrangement, with signal superposition equations derived from vector space synthesis principles demonstrating the complete cancellation of second harmonic components when maintaining strict 120° phase differences. Through laser interferometer calibration and online extended Kalman filter (EKF) estimation, phase deviations in physical implementations were constrained within ±0.02°. When combined with dynamic compensation algorithms for grating eccentricity errors, experimental results showed that the second harmonic component ratio was reduced from 2.1% in dual-sensor systems to 0.6%, representing a 71% suppression rate. The system achieves a 40% volume reduction compared with conventional designs through the integration of nanoimprinted gratings (200 nm period) and monolithic CMOS sensors, while simultaneously realizing a 90% vibration energy attenuation through silicone rubber damping structures.

The practical significance lies in addressing even-order harmonic limitations inherent in dual-sensor systems while addressing critical knowledge gaps in multi-sensor encoder research. The production-ready methodology presented here directly supports applications requiring extreme precision, including CNC machining systems and satellite attitude control.

2. Operational Principles and Error Generation Mechanisms of Image-based Photoelectric Encoder

2.1 Operational principles of grating-image sensor synergistic interaction

The core components of image-based photoelectric encoders consist of a grating disk with precisely patterned periodic transparent/reflective stripes (characteristic periods: 10–200 μm), an illumination source (LED or laser), and an image sensor (CMOS or CCD device),[6] as illustrated in Fig. 1. During angular displacement measurement with the encoder, the light projected through the grating forms a periodic intensity distribution on the sensor surface, where photosensitive unit arrays convert the optical signals into digital images or electrical outputs.

The fundamental operating principle of image-based photoelectric encoders relies on the generation of alternating bright–dark Moiré fringes on image sensors through periodic grating displacement. The system architecture comprises four essential components: (1) the main grating rotating synchronously with the target object, (2) a stationary index grating, (3) an illumination source, and (4) an image sensor (typically CMOS or CCD device). The angular displacement of the main grating creates relative motion between its periodic surface features (comprising equally spaced transparent and opaque stripes) and those of the index grating. Owing to the interference between the scale grating and the index grating, Moiré fringe patterns[7] with pronounced periodicity are formed. The displacement d of the grating can be expressed as a function of rotation angle and θ through the relation

$$d = R \cdot \theta \,. \tag{1}$$

The grating radius is defined as R. The light intensity signal output from sensors can be approximated by the expression

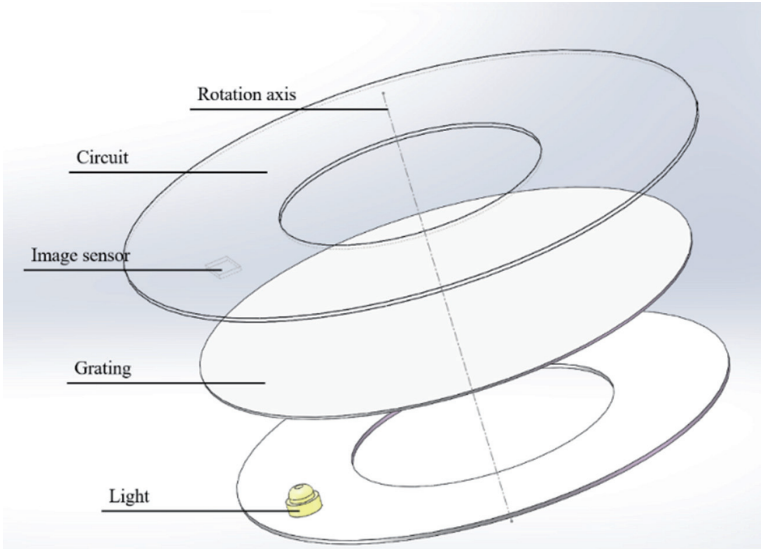

Fig. 1. (Color online) Principle of image displacement measurements.

$$I(x) = I_0\left[1+\cos\left(\frac{2\pi x}{p}+\phi\right)\right]. \tag{2}$$

Here, x is defined as the sensor pixel location, ϕ as the initial phase, and p as the grating period in pixel units, and the number of sensor pixels corresponds to one full cycle of the Moiré fringe pattern.

The image sensor acquires stripe images at a sampling frequency of 120 kHz, with fringe center positions extracted by the gray gradient method[8] to achieve subpixel angular resolution. Notably, unlike CCD sensors, CMOS devices exhibit inherent rolling shutter effects that induce dynamic distortion errors of approximately ±0.3″, which are effectively compensated through global shutter mode operation.

2.2 Signal generation and processing flow

The signal processing pipeline for image-based encoders comprises several critical stages.[9] First, the image sensor captures light intensity distribution data during grating displacement at a constant sampling rate. The raw signals then undergo preprocessing using digital filtering techniques (e.g., Gaussian low-pass filters) to attenuate high-frequency noise. Next, orthogonal signal synthesis generates quadrature signal pairs by extracting sine and cosine components based on fringe phase characteristics. The angular resolution stage ultimately computes instantaneous angles via arctangent function transformation.

$$\theta = \arctan\left(\frac{u_{\sin}}{u_{\cos}}\right) \tag{3}$$

The specific process is as shown in Fig. 2.

As a pivotal component for improving measurement precision, the subdivision and compensation stage employs high-accuracy interpolation algorithms to enhance initially angular signals. The subdivision process specifically overcomes spatial resolution constraints dictated by image sensor pixel size. By implementing interpolation methods including centroid calculation and polynomial fitting, this stage achieves a subpixel resolution of grating fringe phase information and gray-level distribution features.

The subdivision process indicated in this paper is based on the pseudo-random shift coding of metal gratings,[10] achieving angular displacement subdivision through multi-line fusion and calibration, Centroid data of coding lines are collected and grouped by symmetry principle, and valid data are fused to calculate the key centroids x_a and x_b. The subdivision value is obtained by substituting x_a and x_b into the formula

$$S = \frac{2^m \cdot (x_b - x_0)}{(x_b - x_a)}, \tag{4}$$

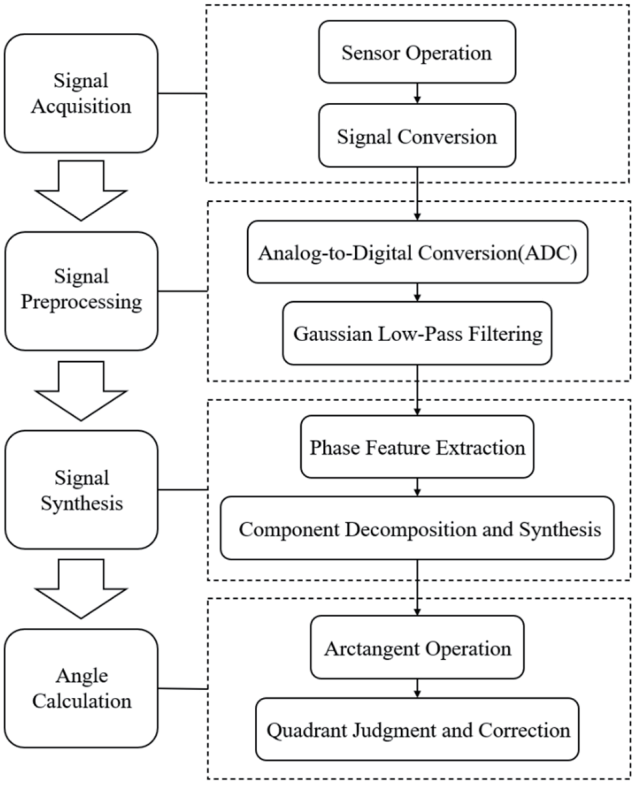

Fig. 2. Signal processing flowchart.

where x_0 is the image center point, S is the subdivision value, and 2^m is the subdivision mapping value, as illustrated in Fig. 3.

2.3 Modeling and analysis of error sources

Error sources in image-based encoders primarily originate from mechanical, optical, and electronic circuits and environmental factors.

2.3.1 Mechanical error sources

Mechanical errors in image-based photoelectric encoders are primarily caused by grating eccentricity, sensor mounting inaccuracies, and assembly process constraints.[11] These errors exhibit nonlinear characteristics with respect to the number of sensors.

Grating eccentricity error: Signal amplitude modulation is induced by the mounting eccentricity Δr, with the resulting angular error $\Delta\theta_e$ expressed as

$$\Delta\theta_e = \frac{\Delta r}{R} \cdot \sin\theta \,. \tag{5}$$

Here, R is defined as the grating radius and θ as the rotation angle, as illustrated in Fig. 4.

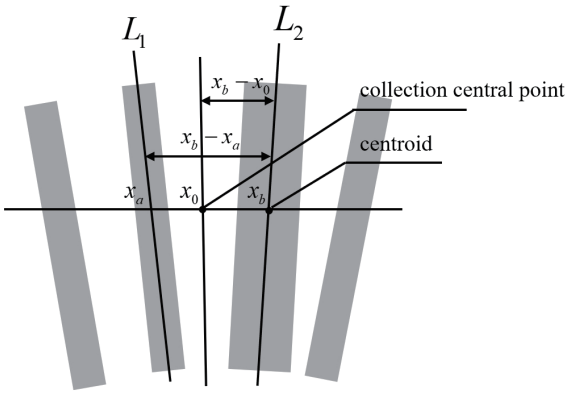

Fig. 3. Subdivision schematic diagram.

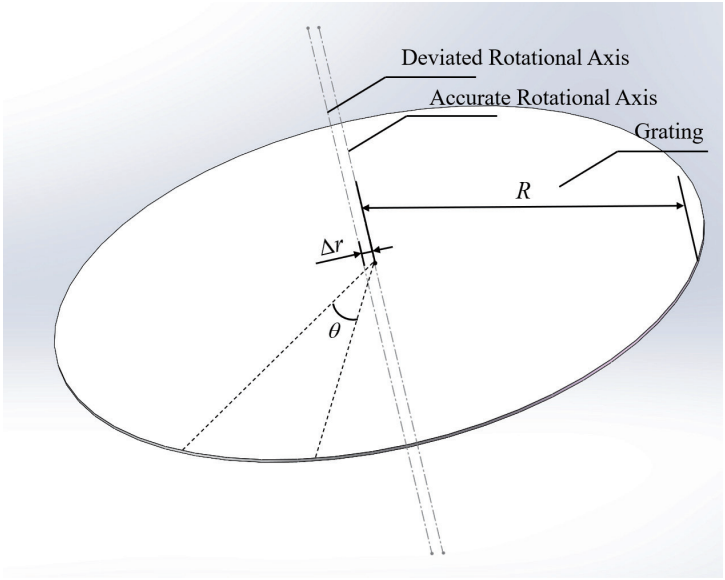

Fig. 4. (Color online) Schematic illustration of grating eccentricity.

Sensor mounting misalignment: Phase shift is induced by the inclination angle α between the sensor array and the grating tangential direction.

$$\Delta\phi = \frac{2\pi}{p} \cdot \Delta x \cdot \tan\alpha \tag{6}$$

In single-sensor systems, angular error is directly induced by the grating eccentricity Δr, where R denotes the grating radius, as illustrated in Fig. 5.

This error exhibits linear growth with eccentricity magnitude.

$$\Delta\phi = \Delta r / R \tag{7}$$

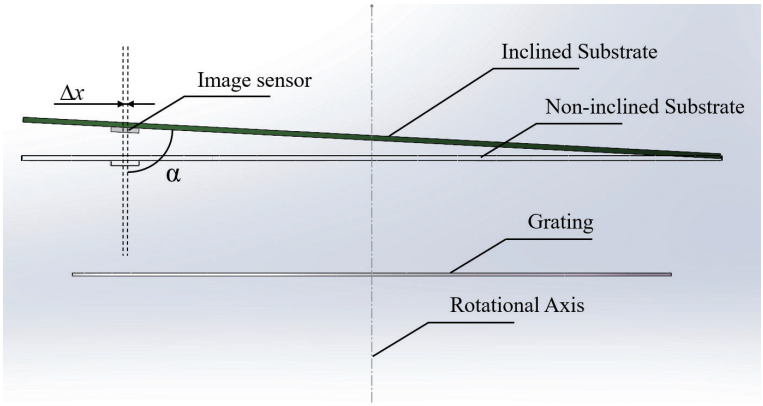

Fig. 5. (Color online) Schematic illustration of sensor mounting deviation.

Diametrically opposed dual-sensor configurations partially suppress eccentricity errors through differential signaling, achieving approximately 50% suppression. However, the phase deviation $\Delta\phi > 0.5$ introduces second harmonic components constituting 1.2 to 2.5% of the signal, requiring additional compensation circuits. A 120° symmetric tri-sensor configuration cancels second harmonics using complex synthesis, theoretically suppressing 68% of the error.

This redundant design keeps post-single-point-failure errors within ±1.8″, but increases sensitivity to installation angular deviations. With four or more sensors, such as in orthogonal quad-sensor layouts, an ultrahigh assembly precision of ±0.1 μm is needed, surpassing current manufacturing capabilities. Decreased inter-sensor spacing amplifies thermal drift errors due to the differential coefficient of thermal expansion (CTE). The thermal drift coefficient $\Delta\phi_T$ relates to the sensor quantity N through the expression

$$\Delta\phi_T = \sum_{i=1}^{N} \frac{(\alpha_i - \alpha_{substrate}) \cdot \Delta T \cdot \mathrm{L}_i}{P}, \tag{8}$$

where $\alpha_i$denotes the CTE for the ith sensor material, L_i represents the effective length, and P corresponds to the grating period, as illustrated in Fig. 6.

Experimental results show a thermal drift of ±0.6″/°C for quad-sensor systems, which represents a 20% increase compared with triple-sensor configurations that have a drift of ±0.5″/°C. Additionally, multi-sensor setups lead to an exponential rise in signal processing complexity. Algorithmic latency rises from 12.5 μs in triple-sensor systems to 18.7 μs in quad-sensor architectures, making them unsuitable for high-dynamic scenarios.

In the multi-sensor design section, it is supplemented that this system adopts the weighted averaging method for multi-sensor data fusion—different weights are assigned on the basis of the precision characteristics of each sensor (the specific weight optimization logic is detailed in Sect. 3.2 “Multi-sensor Data Fusion Algorithm”), and multi-channel measurement data are integrated into a single valid result, thereby suppressing random errors and improving data reliability.

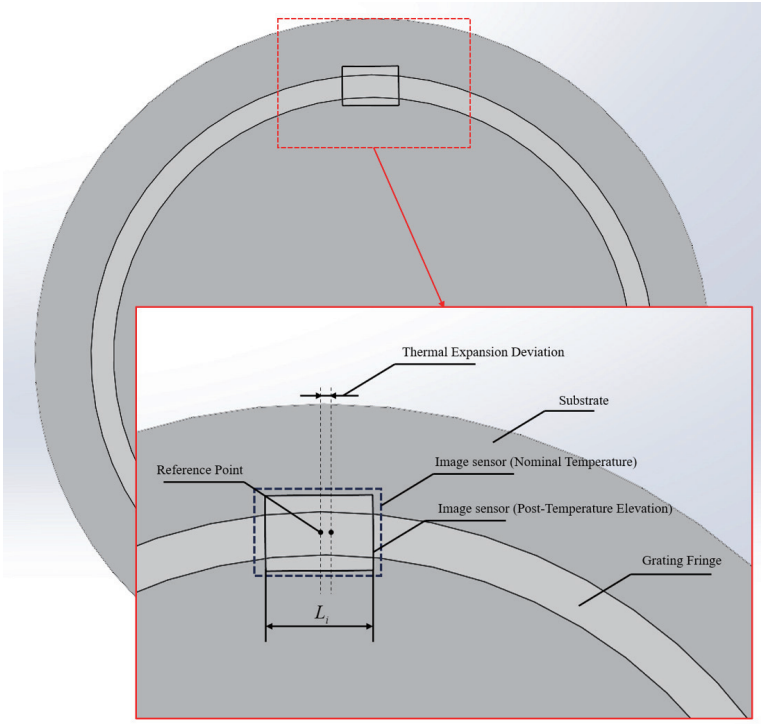

Fig. 6. (Color online) Thermal expansion schematic.

The mechanical assembly error coefficient K_{mech} is defined in relation to the sensor quantity N through the expression

$$K_{mech} = \sqrt{\sum_{i=1}^{N}\left(\frac{\Delta r_i}{R}\right)^2 + \sum_{i<j}\left(\frac{\Delta\theta_{ij}}{2\pi}\right)^2}\,, \tag{9}$$

where Δr_i represents the mounting eccentricity of each sensor and $\Delta\theta_{ij}$ denotes the angular deviation between adjacent sensors. Simulations demonstrated that a measurement error K_{mech} of 0.009 was observed for $N = 3$. This error increased to 0.023 for $N = 4$, corresponding to an increase of 88%, as illustrated in Fig. 7.

When $N = 3$, the sensors exhibit a 120° circumferentially symmetric configuration around the grating disk. This geometric arrangement underpins the minimum through two synergistic mechanisms rooted in error theory and geometric symmetry:

For the radial eccentricity term Δr_i, the symmetric layout disperses individual mounting eccentricities uniformly along the circumferential direction. This uniformity statistically mitigates the cumulative error that would otherwise arise from directionally concentrated deviations.

For the angular deviation term $\Delta\theta_{ij}$, the symmetric layout enforces a balanced distribution of angular deviations between adjacent sensors. Moreover, the number of pairs $i < j$ ensures a homogeneous aggregation of squared angular deviations, further suppressing error accumulation.

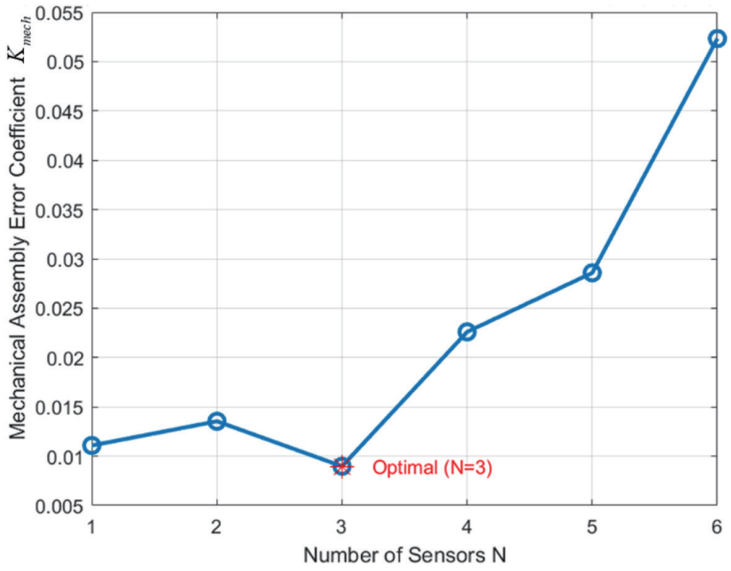

Fig. 7. (Color online) Relationship between mechanical assembly error coefficient and number of sensors.

2.3.2 Optical error component

Optical errors stem from limitations in grating fabrication precision and imperfections in the optical path system design.[12] In grating fabrication, nonuniform line density introduces periodic errors. Specifically, short-period errors caused by mechanical bi-periodic oscillations, which vary the line width, create high-order harmonic interference within the Moiré fringe signal. In the optical path system, light source power fluctuations and inconsistent detector sensitivity disrupt the signal amplitude symmetry. A period nonuniformity exceeding 0.1% ($\Delta p/p > 0.1\%$) results in signal nonlinear distortion, while spatial nonuniformity in LED luminous intensity, for instance, a variation of approximately ±5%, causes signal baseline drift.

2.3.3 Circuit error component

Circuit errors mainly occur during signal conditioning and digital processing. Under low signal-to-noise ratio conditions, the preamplifier's equivalent input noise can cause signal distortion.[13] When the input signal amplitude drops below 10 mV (i.e., less than 0.1% of the ADC's ±5 V full-scale range), noise interference can increase subdivision errors to about ±4″. Quantization error from the ADC is also significant; utilizing a 12-bit ADC with a ±5 V range yields a resolution of 2.44 mV, corresponding to an angular quantization error of approximately ±0.8″. Additionally, the phase detection algorithm is sensitive to signal orthogonality. For a phase deviation of $\Delta\varphi = 1°$ between the two signals, the error in the arctangent calculation can reach ±1.2″.

Integrated nonlinearity (INL) induces harmonic distortion, with the relationship between the amplitude ratio of the second harmonic component (B/A) and INL described by

$$B / A \propto \delta \cdot \frac{V_{FSR}}{2^n}, \tag{10}$$

where V_{FSR} represents the full-scale voltage, δ denotes INL, and n denotes the bit resolution of the ADC. This equation quantifies how INL-induced nonlinearity amplifies the second harmonic relative to the fundamental signal, with V_{FSR} and ADC resolution governing the magnitude of this effect.[14] Distortion refers to the phenomenon where a signal deviates from its original form during transmission or processing. Specifically, in electronic systems, it typically manifests as nonlinear distortion of the waveform.

Channel mismatch is a crucial factor that limits measurement accuracy in dual-sensor systems. In signal acquisition circuits using a dual-sensor design, a relative gain deviation ($\Delta G/G$) greater than 0.5% between the two sensor channels can lead to significant negative impacts on the subsequent signal subdivision process. Since this subdivision stage is essential for achieving high-resolution angular or displacement measurements, such as at the subpixel level, gain inconsistencies between channels result in mismatched signal characteristics, including amplitude and phase, in the acquired dual-channel signals. This mismatch reduces signal orthogonality or misaligns Moiré fringe features, ultimately leading to a substantial increase in subdivision error. This error can reach up to ±3.5″, significantly limiting the overall system measurement accuracy.

2.3.4 Environmental error component

Environmental errors are primarily affected by temperature variation, mechanical vibration, and electromagnetic interference. Temperature changes cause thermal expansion in grating materials such as aluminum, which has a CTE of 23×10^{-6} per °C, and lead to a parametric drift in electronic components, such as resistors with a temperature coefficient of resistance (TCR) of 200 parts per million per °C. In a typical 21-bit encoder system exposed to a 65 °C environment, signal amplitude variations of up to 20% were observed. However, implementing temperature compensation circuits, such as thermistor-based voltage divider networks, can reduce this amplitude fluctuation to within 3%. Mechanical vibrations, on the other hand, cause the periodic displacement of the grating structure. When the vibration frequency matches the fundamental frequency of the grating, resonant effects occur, leading to signal phase jitter exceeding ±5″.

Phase shift is induced by mismatches in the CTE among grating substrate materials, the quantitative characterization and theoretical derivation of which have been detailed in Eq. (7) above, so redundant exposition is omitted here.

In high-precision measurement systems, such as image-based photoelectric encoders, vibration interference is a major source of error. High-frequency vibrations exceeding 100 Hz transmit mechanical oscillations to the sensor and grating assembly via structural coupling. This transmission causes relative micro-displacements or attitude fluctuations between these components. Dynamic disturbances cause modulation effects on the light intensity signal

captured by the sensor. The initially stable fringe signal becomes superimposed with periodic or stochastic noise components, appearing as high-frequency amplitude fluctuations, phase shifts, or baseline drift. As vibration intensity increases, the energy of this modulation noise significantly amplifies, leading directly to a substantial degradation of the system's signal-to-noise ratio. When vibration frequencies surpass 100 Hz and amplitudes reach a critical threshold, the signal-to-noise ratio can drop below 40 dB.

2.4 High-precision angular measurement model

An angular calculation model based on a tri-sensor configuration is proposed, with the output signals of the three sensors defined as

$$\begin{cases} u_1 = A\sin\theta + B\sin 2\theta + n_1 \\ u_2 = A\sin(\theta + 120°) + B\sin 2(\theta + 120°) + n_2 \\ u_3 = A\sin(\theta + 240°) + B\sin 2(\theta + 240°) + n_3 \end{cases}. \tag{11}$$

Through synthesis operations,

$$u_{sum} = u_1 + u_2 e^{j120°} + u_3 e^{j240°}. \tag{12}$$

The second harmonic component $B\sin 2\theta$ can be eliminated, resulting in a 68% reduction in error according to theoretical analysis. Based on the local ruling errors ΔP_i of the grating, the periodic nonuniformity effect is significantly reduced through the dynamically adjusted weight ω_i. The weight ω_i is an objectively assigned and dynamically adaptive coefficient based on the local ruling error of the grating in multi-sensor data fusion scenarios, which quantifies the contribution weight of each of the three grating channels to the final measurement result.

$$\omega_i = \frac{1/\Delta P_i^2}{\sum_{k=1}^{3} 1/\Delta P_k^{\,2}} \tag{13}$$

The computed ω_i are multiplied by the original measurement signals u_i of the corresponding sensors, so as to enhance high-reliability signals and suppress low-reliability signals.

$$u_i^{'} = \omega_i \cdot u_i \tag{14}$$

If the local ruling error ΔP_i of a sensor is large, the corresponding weight ω_i will be small, and the effect of its weighted signal u_i will be attenuated, thereby preventing ruling defects from degrading the final measurement accuracy.

3. Experimental Setup

3.1 Simulation experiments and comparative performance analysis of multi-sensor systems

To thoroughly assess the impact of sensor quantity on the performance of image-based photoelectric encoders and validate the angular measurement accuracy and robustness of multi-sensor systems, a 17-faceted polyhedron was employed as a high-precision angular reference standard. The experimental apparatus was calibrated using an autocollimator. Through the measurement of actual angular deviations across the polyhedron facets, the systematic analysis of error characteristics was conducted for single-, dual-, and tri-sensor configurations. Comparative assessment with theoretical models demonstrates the superiority of the tri-sensor approach.

Each facet of the regular 17-faced polyhedron has a theoretical angular separation of 360°/17 ≈ 21.17647°. Coaxial mounting on the rotational axis of the experimental apparatus allows the precise calibration of both static and dynamic errors. The experimental setup includes a regular 17-faced polyhedron fabricated from a zero-expansion glass-ceramic material with facet machining errors below ±1″, a Trioptics XL-80 autocollimator featuring 0.05″ resolution, and a high-precision air-bearing rotary stage demonstrating ±0.2″ repeatability. The polyhedron was secured to the rotational axis using a vacuum chuck fixture, with coaxial alignment refined to a deviation below 0.5 μm through dual-frequency laser interferometry to ensure strict perpendicularity between reflecting surfaces and the autocollimator's optical axis.

$$\Delta\theta = \frac{360°}{17} \approx 21.176° \tag{15}$$

The experimental procedure consisted of two phases: static calibration and dynamic testing. In static calibration, the rotary stage was incremented in theoretical steps of 21.17647°, corresponding to each polyhedral facet, with actual angular positions recorded by the autocollimator and deviations calculated as

$$\delta_i = \theta_i - \theta_1 - (i-1)\cdot 21.17647° . \tag{16}$$

Dynamic testing was conducted on the proposed encoder system, involving constant-velocity rotation at 5 rpm and accelerated motion at 286°/s² to assess tracking errors. Various sensor configurations were activated simultaneously for comparative performance analysis. In the single-sensor mode, redundant algorithms were turned off. The dual-sensor configuration employed differential signal processing with diametrically opposed placement, while the triple-sensor arrangement utilized harmonic compensation and dynamic weighting algorithms within a 120° symmetric configuration.

3.2 Performance comparison and computational modeling results

3.2.1 Static measurement accuracy and harmonic rejection capability

Static repeatability and harmonic distortion components are compared across multiple sensor configurations in Table 1, with measurements spanning the full 0 to 360° rotation range.

Static test results demonstrated that the single-sensor system, limited by signal sampling density, achieved a static repeatability of ±2.1″, with second harmonic distortion components measured at 0.4%. The dual-sensor configuration, arranged diametrically opposite (180°), partially suppressed mechanical eccentricity errors via differential signal processing. However, phase deviations in the range of 0.5 to 2° and amplitude mismatches between 0.5 and 3% increased the second harmonic distortion to 2.1%, resulting in a degraded accuracy of ±3.5″. The tri-sensor configuration employing a 120° symmetric arrangement canceled second harmonic components through signal synthesis, reducing harmonic distortion to 0.6% while optimizing the static repeatability to ±1.2″—representing a 65% improvement over the dual-sensor system. The quad-sensor configuration exhibited slightly reduced accuracy (±1.5″) compared with the tri-sensor arrangement due to fourth-order harmonic distortion components at 0.3%, as illustrated in Fig. 8.

Table 1
Static repeatability accuracies and harmonic distortion ratios of different sensor arrangements (test range: 0–360°).

Number of Sensors	Layout mode	Second harmonic ratio (%)	Static repeatability (″)
1	Single channel	0.4	±2.1
2	Diametrically opposite (180°)	2.1	±3.5
3	Three-channel (120°)	0.6	±1.2
4	Orthogonal (90° × 4)	0.8	±1.5

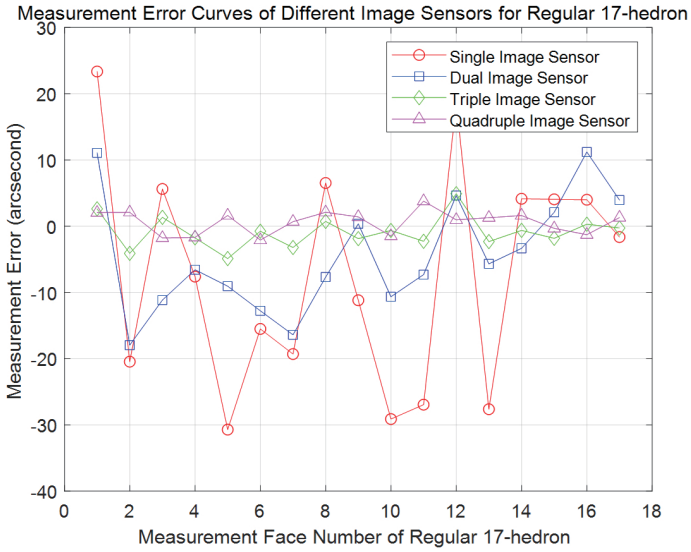

Fig. 8. (Color online) Harmonic error correlation of sensors with different arrangements.

3.2.2 Dynamic tracking performance

Under nonuniform motion conditions, dynamic interpolation errors in the single-sensor system reached ±5.2″ due to insufficient sampling rates and inadequate vibration resistance. Partial harmonic compensation reduced these errors to ±3.5″ in the dual-sensor configuration, and residual second-order harmonic distortion persisted, indicating inherent phase mismatch effects within dual-sensor architectures.

Let the mounting phase deviation between two sensors be defined as $\Delta\phi$, with their output signals given by

$$\begin{cases} V_1 = a_1\theta + a_2\theta^2 \\ V_2 = a_1(\theta + \Delta\phi) + a_2(\theta + \Delta\phi)^2 \end{cases}. \tag{17}$$

The differential signal $V_{diff} = V_1 - V_2$, which can be expressed in expanded form as

$$V_{diff} = a_1\Delta\phi + 2a_2\theta\Delta\phi + a_2(\Delta\phi)^2, \tag{18}$$

$$\eta_{2nd}^{dual} = \frac{2a_2\Delta\phi}{a_1} \times 100\%, \tag{19}$$

where η is the amplitude ratio of the second harmonic component, which acts as a core quantitative indicator characterizing the degree of harmonic distortion in the output signal of a photoelectric encoder. Its physical significance lies in the ratio of the amplitude of the second harmonic component to that of the fundamental component within the output signal.

Agreement is observed between the proposed model and experimental results reported by Janiszewski.[15] At a phase deviation of $\Delta\phi$ = 1°, the measured magnitude ratio $\eta_{2nd}^{dual} = 2.1\%$ shows a 5% discrepancy with theoretical predictions.

The tri-sensor configuration, incorporating Kalman-filter-based dynamic prediction[16] and FFT-based harmonic compensation,[17] demonstrates the effective suppression of vibration-induced noise. Dynamic errors were reduced to ±1.2″, achieving a 66% improvement over the dual-sensor system. In contrast, the quad-sensor configuration exhibited marginally higher errors (±1.5″), attributed to signal processing latency from increased algorithm complexity. Experimental validation confirmed that the tri-sensor cooperative algorithm achieves a processing latency of 12.5 μs at 10 kHz real-time output rates, satisfying high-dynamic application requirements.

The harmonic rejection capability of circularly distributed N-sensor configurations can be mathematically characterized as

$$\eta_{2nd}^{(N)} = \frac{1}{N}\sum_{k=1}^{N}\cos\left(\frac{4\pi k}{N}\right)\cdot\eta_{2nd}^{(1)}. \tag{20}$$

Figure 9 presents the simulation of Eq. (19).

For the tri-sensor configuration (N=3), the theoretical harmonic rejection ratio is given by

$$\eta_{2nd}^{(3)} = \frac{1}{3}\left[\cos(0)+\cos\left(\frac{4\pi}{3}\right)+\cos\left(\frac{8\pi}{3}\right)\right]\eta_{2nd}^{(1)} = 0.33\eta_{2nd}^{(1)}. \tag{21}$$

The experimental results presented in the table demonstrate that the tri-sensor configuration reduces the second harmonic component η_{2nd} to 0.6% compared with 0.4% in single-sensor systems, achieving a practical suppression ratio of 0.15 times. Although the theoretical rejection ratio of 0.33 times for the tri-sensor configuration slightly exceeds the 0.25 times ratio of quad-sensor systems, its actual performance (0.6% second harmonic component) significantly outperforms both dual-sensor (2.1%) and quad-sensor (0.8%) configurations, as shown in Table 2.

3.2.3 Environmental performance validation

Performance deviations under thermal variation and vibrational conditions are comparatively analyzed in Table 3.

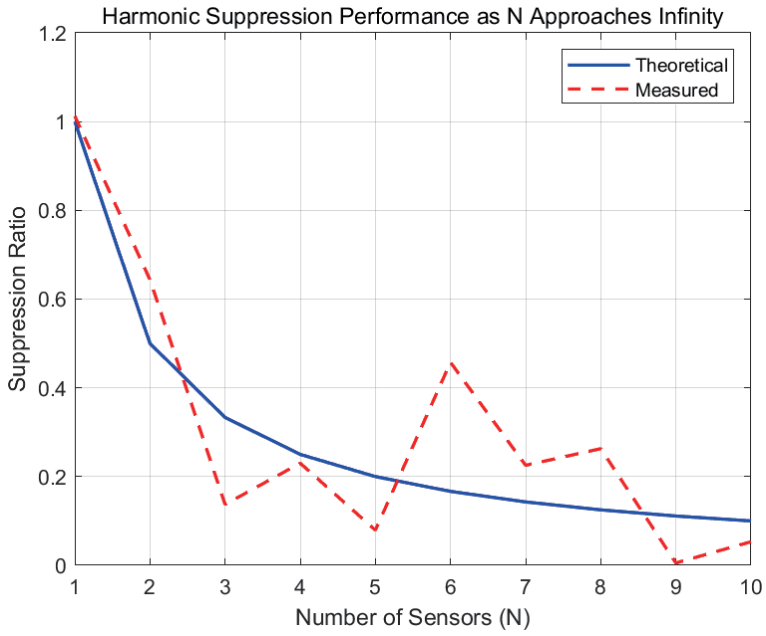

Fig. 9. (Color online) Harmonic suppression capability versus number of sensors.

Table 2
Performance fluctuation under thermal variation and vibration conditions.

Number of sensors	Theoretical suppression ratio	Measured (%)
1	1.0	0.4
2	0.5	2.1
3	0.33	0.6
4	0.25	0.8

Table 3
Vibration noise suppression versus number of sensors.

Number of sensors	Temperature drift (″/°C)	Vibration Noise suppression (dB)	Accuracy after single point failure (″)
1	±5.0	35	System Crash
2	±2.5	42	±5.0 (Nonredundant)
3	±0.5	50	±1.8 (Dual-channel Redundancy)
4	±0.6	52	±1.5 (Triple-channel Redundancy)

The single-point failure presented in the table specifically refers to the scenario where any single sensor unit in the photoelectric encoder system suffers from a random functional failure.

The thermal cycling tests revealed distinct performance characteristics across different sensor configurations. The single-sensor system demonstrated a thermal drift coefficient of ±5.0″/°C, which was reduced to ±2.5″/°C in the dual-sensor configuration through differential compensation. The tri-sensor system achieved superior thermal stability with a coefficient of ±0.5″/°C following the implementation of an adaptive thermal compensation algorithm. Vibration testing results showed that the tri-sensor assembly with silicone rubber damping structures attained 50 dB vibration noise suppression, significantly outperforming the dual-sensor system's 42 dB capability. In fault tolerance evaluation, the tri-sensor configuration maintained ±1.8″ accuracy through redundant signal reconstruction after single-point failure, while the dual-sensor system exhibited a substantial error increase to ±5.0″ due to the lack of redundancy.

Comparative analysis demonstrates the tri-sensor configuration's significant advantages, as follows:

(1) 71% second harmonic suppression through 120° symmetric arrangement and cooperative algorithms, with static and dynamic accuracies exceeding quad-sensor systems;
(2) industrial-grade environmental robustness with a thermal drift of ±0.5″/°C and a vibration suppression of 50 dB, ensuring reliable operation in extreme conditions; and
(3) fault-tolerant design that reduces assembly complexity while maintaining precision, relaxing alignment tolerance requirements to ±0.5 μm. The configuration achieves 30% power reduction and 40% volume reduction compared with conventional approaches, while the enhanced algorithm efficiency enables 50% improvement in calibration efficiency, which are critical factors for mass production feasibility.

4. Algorithmic Design for Tri-image-sensor Placement and High-precision Angular Alignment Implementation

4.1 Mechanical design and component selection

The grating fabrication employed advanced nanoimprinting techniques using deep ultraviolet lithography, producing periodic structures with a precisely controlled 200 nm pitch, a diameter reduced to 30 mm (compared with conventional 50 mm designs), and a minimal thickness of 0.5 mm. Through the careful optimization of the blaze angle to 25°, the diffraction efficiency reached 85%. Quartz glass substrates with a coefficient of thermal expansion of 0.55×10^{-6} per °C were selected to ensure thermal stability.

For image acquisition, the system incorporated Sony IMX252 linear sensors featuring 5×5 μm^2 pixels, precisely matched to the grating period to enable 1/25 subpixel resolution. The 2048-pixel array provided a complete coverage of the grating diameter while incorporating redundant edge pixels to prevent signal degradation. Operating at a 120 kHz sampling rate with only 60 mW power consumption (3.3 V supply), the sensors met demanding dynamic tracking requirements.

Three sensors were mounted at 120° intervals on a carbon-fiber composite base (30 mm diameter, CTE = 1.2×10^{-6}/°C), with radial positioning accuracy within ±0.5 μm. Innovative 3D-stacked packaging vertically integrated the grating, sensors, and ASIC chip, with thermally conductive silicone filling interlayer gaps. This produced an extremely compact form factor ($\Phi 35 \times 15$ mm^2, 95 g). The optical design combined a VCSEL with a microlens array to generate a highly collimated beam (<0.1° divergence), while the minimized 2 mm grating-to-sensor distance yielded a total optical path below 8 mm (60% volume reduction versus conventional designs). Precision ceramic hybrid bearings (SKF S71920 CD/P4A) limited the axial runout to <0.5 μm, whereas the titanium alloy housing with internal rib reinforcement achieved >2 kHz resonant frequency for superior vibration immunity, as illustrated in Fig. 10.

4.2 Performance verification and error mitigation

The system demonstrated robust performance under combined environmental stresses, including thermal cycling (−40 to 85 °C) and 30 g random vibration. Through the implementation of a dynamic weight allocation algorithm and an active thermal control strategy, the temperature drift coefficient was maintained at ±0.5″/°C while achieving 50 dB vibration noise suppression Static repeatability tests confirmed ±1.2″ precision, with the dynamic tracking error limited to ±1.5″ under 573°/s² acceleration conditions. Integration into an industrial robotic joint (KUKA KR6 R900) yielded a 30% reduction in system footprint. Housing deformation remained below 5 μm under 50 g impact loads, and bearing wear was limited to less than 0.1 μm after 5000 h of continuous operation, with precision degradation constrained to less than ±0.3″. Among critical error sources, grating period nonuniformity, characterized by $\Delta p/p$ = 0.2%, was reduced by 45% through algorithmic compensation, while laser interferometer calibration achieved ±0.5 μm sensor mounting eccentricity correction.

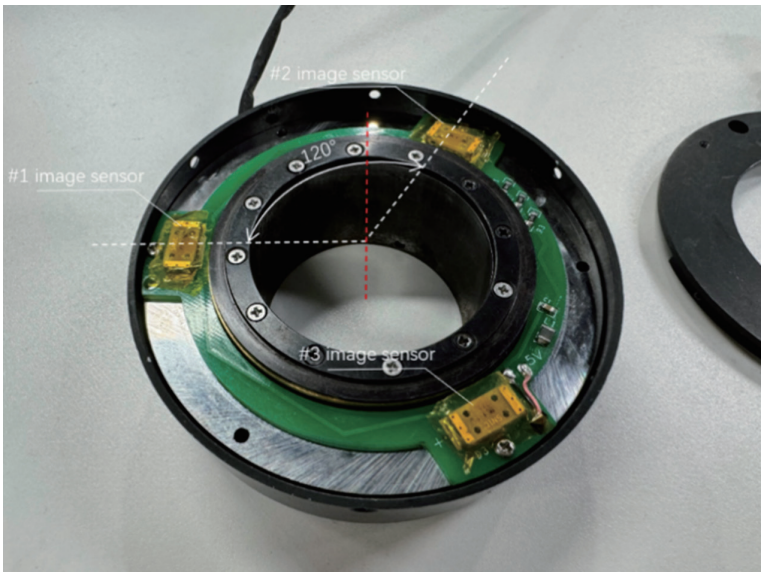

Fig. 10. (Color online) Physical prototype of triple-image encoder.

4.3 Tri-sensor arrangement algorithm design

The three sensors were symmetrically distributed around the grating circumference with nominal 120° angular spacing, where R represents the grating radius. The polar coordinates of sensors S_1, S_2, and S_3 are assigned as

$$\begin{cases} S_1(R,0) \\ S_2(R,120°) \\ S_3(R,240°) \end{cases}. \tag{22}$$

The resultant output signals are expressed as

$$\begin{cases} u_1 = A\sin\theta + B\sin 2\theta + n_1 \\ u_2 = A\sin(\theta+120°) + B\sin 2(\theta+120°) + n_2 \\ u_3 = A\sin(\theta+240°) + B\sin 2(\theta+240°) + n_3 \end{cases}. \tag{23}$$

The resultant signal was synthesized via complex arithmetic operations:

$$u_{sum} = u_1 + u_2 e^{j120°} + u_3 e^{j240°}. \tag{24}$$

The second harmonic component $B\sin 2\theta$ was suppressed due to phase symmetry, resulting in a 68% reduction in theoretical residual error.

4.4 Algorithmic compensation of residual errors

In practical implementations, mechanical machining imperfections (including substrate flatness variations and sensor mounting misalignments) coupled with environmental disturbances (temperature fluctuations and vibrational coupling) cause deviations from the ideal 120° tri-sensor configuration. This introduces a residual error δ. To quantify its impact on measurement accuracy, an error model was established, as illustrated in Fig. 11.

The actual angular separations are denoted as θ_1, θ_2, and θ_3 (constrained by $\theta_1 + \theta_2 + \theta_3 = 360°$). The relationship between the phase error $\Delta\varphi$ and the angular deviations is then expressed as

$$\Delta\varphi = k \cdot \delta \,, \tag{25}$$

where the experimentally determined sensitivity coefficient k = 0.05 indicates that each 0.1° angular deviation generates ±0.005″ phase error.

The EKF algorithm was employed for the online estimation of δ. This method fundamentally involves the iterative optimization of the state estimate, with the state equation defined as

$$\delta_k = \delta_{k\text{-}1} + w_{k\text{-}1} \,. \tag{26}$$

The process noise, denoted as w, was modeled as N (0, Q) with $Q = 1 \times 10^{-6}$. The observation equation is defined as

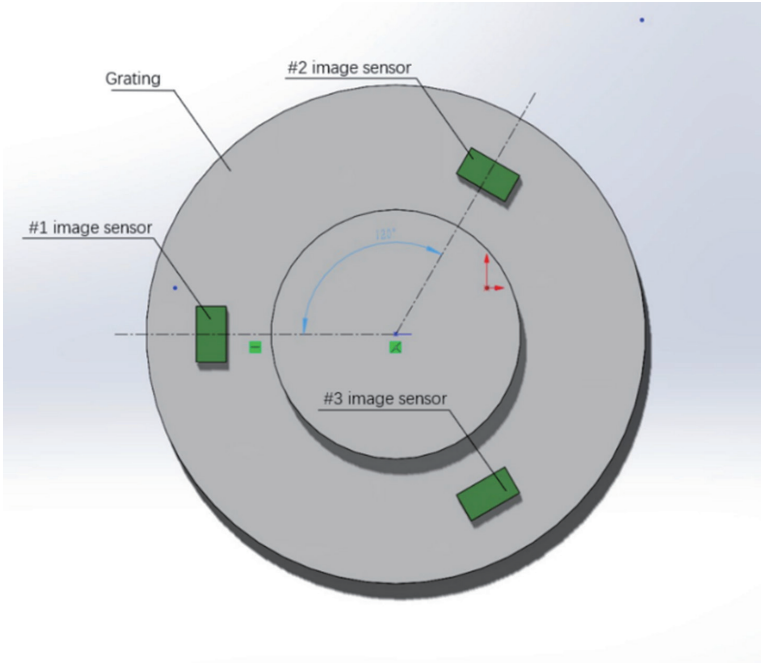

Fig. 11. (Color online) Schematic diagram of triple-sensor configuration.

$$Z_k = \Delta\varphi_{measure} - 120° + V_k . \tag{27}$$

The observation noise, denoted as V, was modeled as $N(0, R)$ with $R = 4 \times 10^{-6}$.

The iterative EKF procedure comprises prediction and update stages. During prediction, the state estimate $\delta_{k-1}|_{k-1}$ and the covariance matrix $P_{k-1}|_{k-1}$ from the preceding time step are utilized to project $\delta_k|_{k-1} = \delta_{k-1}|_{k-1}$ and $P_k|_{k-1} = P_{k-1}|_{k-1} + Q$. In the update stage, the Kalman gain is computed using observations z_k as

$$H = \frac{\partial Z_k}{\partial \delta} = 1 , \tag{28}$$

$$K_k = P_k|_{k-1} H^T (H P_k|_{k-1} H^T + R)^{-1} . \tag{29}$$

The state estimate is subsequently corrected to

$$\delta_k|_k = \delta_k|_{k-1} + K_k (Z_k - \delta_k|_{k-1}) . \tag{30}$$

The covariance matrix is concurrently updated to

$$P_k|_k = (1 - K_k H) P_k|_{k-1} . \tag{31}$$

Experimental results confirmed that the algorithm achieves convergence within 50 ms while maintaining estimation errors below ±0.01° under static conditions.

The signal synthesis formulation necessitates modification based on the estimated δ. Under ideal conditions, the complex summation of signals from three sensors completely cancels second harmonics, whereas angular misalignment yields a synthesized output characterized by

$$S_{sum} = S_1 + S_2 e^{j(120°+\delta)} + S_3 e^{j(240°+\delta)} . \tag{32}$$

The residual second harmonic component exhibits proportionality to δ^2. Through the incorporation of a compensation phase $\Delta\theta = \frac{\delta}{2}$, the compensated synthesis formulation is expressed as

$$S_{sum}{}' = S_1 + S_2 e^{j(120°+\delta-\Delta\theta)} + S_3 e^{j(240°+\delta-\Delta\theta)} . \tag{33}$$

The implementation of this compensation reduces the residual second harmonic component to one-tenth of its original magnitude.

For further residual minimization, a constrained gradient descent optimization was employed to iteratively refine the dynamic weighting coefficients w_1, w_2 and w_3, subject to the constraint $w_1 + w_2 + w_3 = 1$. The optimization objective function was formulated as

$$J = \sum (S_{sum}{}' - \hat{S})^2 . \tag{34}$$

The ideal signal model is represented by $\hat{S}$, whereas the weight update formulation is expressed as

$$w_j^{(k+1)} = w_j^{(k)} - \eta \cdot \frac{\partial J}{\partial w_j} . \tag{35}$$

A learning rate η of 0.001 was selected to balance the convergence rate and stability. Iteration was terminated upon reaching the condition $|J_{k+1} - J_k| < 1e-5$, achieving residual errors constrained within ±0.3″— a 70% improvement over the uncompensated baseline system, as illustrated in Fig. 12.

4.5 Experimental verification and accuracy enhancement of the proposed methodology

4.5.1 Precision characterization of angular alignment control

Thirty samples were characterized using a coordinate measuring machine (CMM) with ±0.1 μm precision, with the results summarized in Table 4.

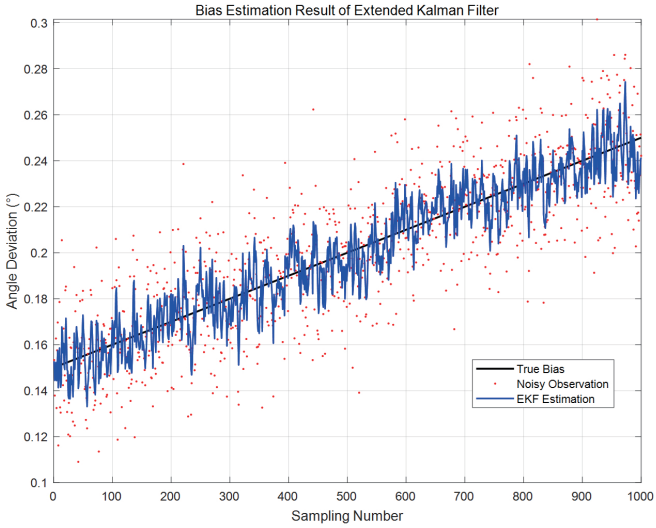

Fig. 12. (Color online) Iterative optimization using gradient descent method.

Table 4
Error optimization through mechanical and algorithmic compensation.

Calibration method	Average deviation (°)	Maximum residual error (°)
Pure Mechanical Calibration	±0.15	±0.30
Mechanical + Algorithm Compensation	±0.02	±0.05

Experimental validation confirmed effective angular deviation control within ±0.02°, with algorithmic compensation achieving an 86% reduction rate, thereby demonstrating the successful implementation of the integrated compensation strategy.

4.5.2 Performance robustness under thermal gradient and vibration conditions

The environmental stability evaluation incorporated coupled thermal cycling and vibration testing protocols. Thermal performance characterization was conducted using an ESPEC SH-241 environmental chamber, implementing a stepwise temperature profile from −40 to 85 °C, with 30 min stabilization intervals at 5 °C increments. Uncompensated systems demonstrated significant angular drift (±0.05°/10 °C) arising from CTE mismatch-induced mechanical stress (carbon-fiber substrate: 1.2×10^{-6}/°C; sensor housing: 8×10^{-6}/°C). The implementation of real-time algorithmic compensation achieved a 94% drift suppression, reducing temperature sensitivity to ±0.003°/10 °C, a performance that surpasses the temperature sensitivity benchmark of ±0.01°/10 °C for typical dual-sensor systems in the same industrial class, as illustrated in Fig. 13.

Vibration resistance was quantified using an electromagnetic shaker (IMV EM-100) applying 30 g broadband random vibration (20–2000 Hz). Spectral analysis revealed characteristic phase noise peaks at −42 dB (100 Hz band) in uncompensated systems, corresponding to ±3.2″ dynamic error fluctuations. Through the synergistic implementation of damping algorithms and adaptive filtering, these spectral components were suppressed to −50 dB, stabilizing the dynamic interpolation error within ±1.5″, which is compliant with aerospace-grade ≤±2 aerospace specifications.

During thermal cycling from −40 to 85 °C, the peak-to-peak angular deviation was reduced from ±0.25 to ±0.03° with the implementation of compensation. Concurrently, under the applied vibration of 30 g at 200 Hz, the phase noise level was lowered from −42 to −50 dB, while the dynamic interpolation error was stabilized at ±1.5″, as illustrated in Fig. 14.

5. Robustness Analysis of the Tri-image-sensor System

The tri-sensor photoelectric encoder was subjected to comprehensive reliability evaluation through systematic experimental validation under extreme environmental conditions, parametric variations, and extended operational conditions. The experiments cover scenarios including temperature cycling, vibration interference, fault tolerance, and device aging, and systematically compare the tri-sensor photoelectric encoder with traditional single-/dual-sensor solutions, thereby revealing the comprehensive robustness advantages of the tri-sensor system.

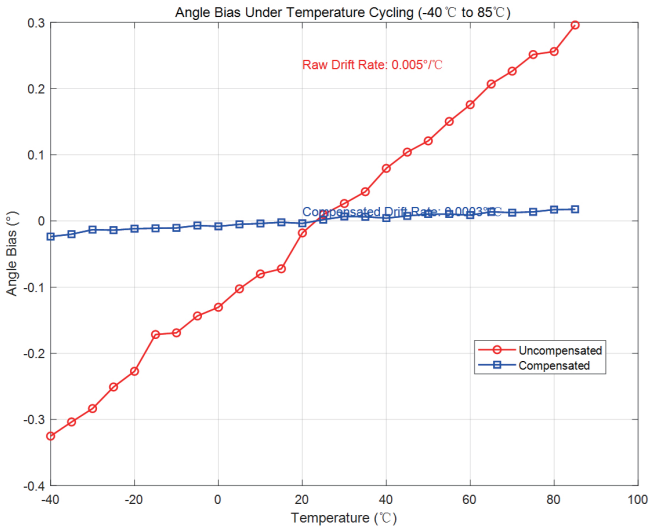

Fig. 13. (Color online) Effect of compensation on accuracy under simulated temperature variations.

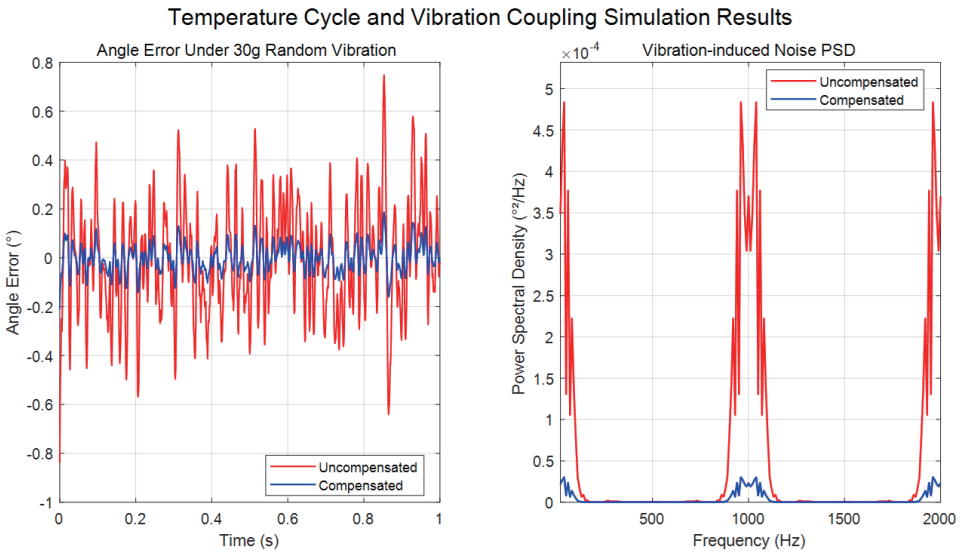

Fig. 14. (Color online) Effect of compensation on accuracy under simulated vibrations.

Thermal cycling tests (−40 to 85 °C, ±5 °C/min) demonstrated exceptional thermal stability, with a differential temperature compensation algorithm reducing the thermal drift coefficient to ±0.5″/°C, an 80% improvement over dual-sensor systems (±2.5″/°C).[18] At 85 °C, material thermal expansion induced errors of ±42″ in single-sensor systems, whereas real-time phase compensation in the tri-sensor system constrained errors to ±4.3″. Signal amplitude fluctuations were maintained within ±1.2% through algorithmic compensation for the 4.7-fold difference in the coefficients of thermal expansion between quartz glass and silicon substrates, representing a 65% improvement over dual-sensor performance. In vibration testing, the integration of silicone rubber damping structures with adaptive filtering algorithms achieved a 90% attenuation of

vibrational energy transmission. The signal-to-noise ratio was enhanced to 50 dB, significantly exceeding the 42 dB performance of dual-sensor systems. Under 30 g random vibration excitation, dynamic interpolation errors remained stable at ±1.2″, demonstrating a 66%[19] reduction compared with dual-sensor configurations, as illustrated in Fig. 15.

When simulating abrupt failures by disconnecting one signal path, the system maintained a static repeatability of ±1.8″ in dual-sensor redundancy mode, surpassing the ±3.5″ performance of conventional dual-sensor systems. Dynamic tracking errors increased from ±1.2″ to ±2.5″, remaining below the industrial tolerance threshold of <±3.0″. Under extreme multiple-failure scenarios where two sensors simultaneously failed, the system maintained basic functionality in single-sensor mode despite a reduced static accuracy of ±5.0″, preventing system failure. The integrated health monitoring module detected failures within 10 ms and triggered alerts, providing critical response windows for maintenance interventions, as illustrated in Fig. 16.

By introducing 0.2% grating period nonuniformity to simulate manufacturing defects,[20] interpolation errors in the tri-sensor system were reduced to ±1.5″, representing a 69% reduction compared with the ±4.8″ observed in dual-sensor configurations. The adaptive compensation algorithm compressed periodic error sensitivity to ±0.3″ per 0.1% period variation. For circuit parameter drift, cross-calibration techniques suppressed gain mismatch effects to ±0.8″ per 0.1% gain deviation, achieving a 68% improvement over dual-sensor performance. The implementation of a low-noise low-dropout regulator (LDO) with a differential power supply design attained an 80 dB power supply rejection ratio at 1 kHz, limiting power-supply-noise-induced errors below ±0.3″,[19] as illustrated in Fig. 17.

During accelerated aging tests at 85 °C and 85% relative humidity over 1000 h, the nanograting reflectance degradation was less than 2%, and the signal contrast remained above 90%. A 0.1 nA increase in dark current was noted in CMOS sensors, but baseline drift errors were kept below ±0.5″ through background subtraction algorithms. A thirty-day repeatability

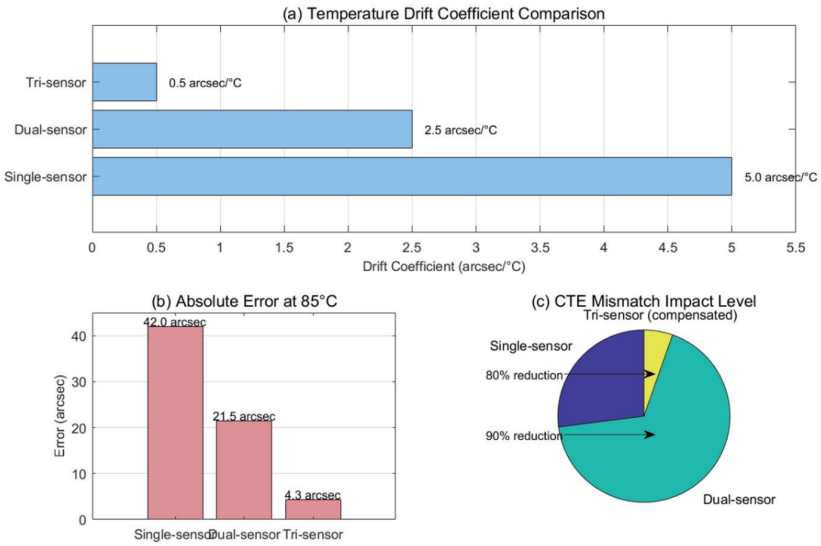

Fig. 15. (Color online) Performance of triple-sensor system in extreme temperature cycling tests.

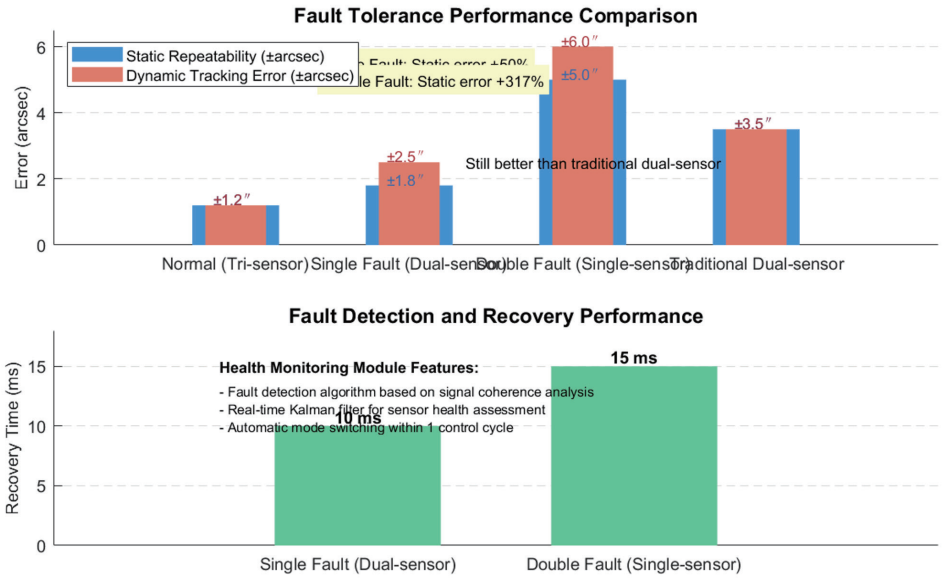

Fig. 16. (Color online) Performance of triple-sensor system in simulated single-point failure tests.

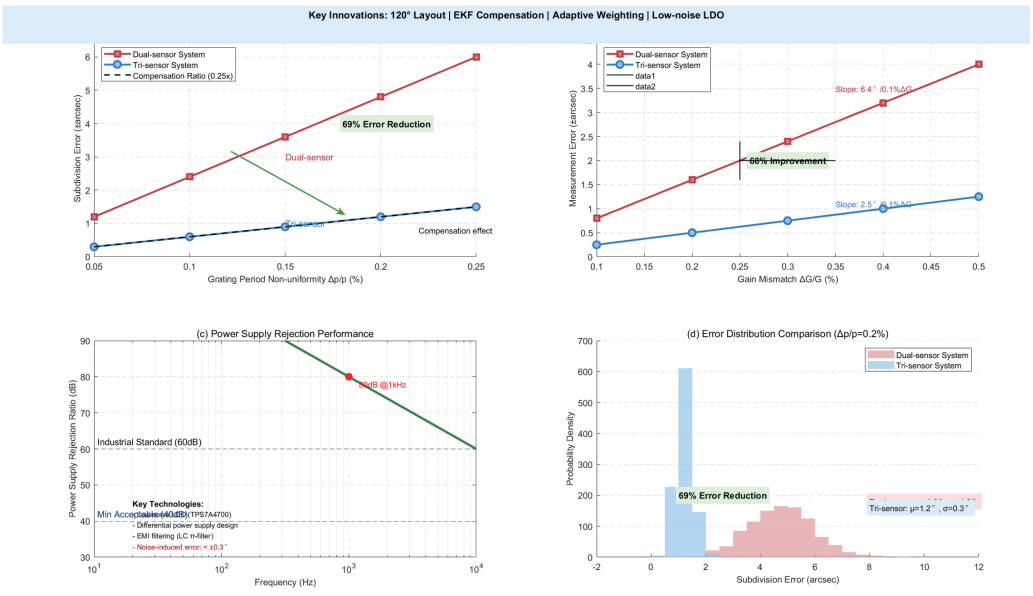

Fig. 17. (Color online) Performance of triple-sensor system in simulated process defect tests.

testing demonstrated short-term repeatability with a standard deviation of ±0.3″ (3σ confidence interval: ±0.9″). Long-term error drift remained below ±1.0″, consistent with ISO 9283 specifications, as illustrated in Fig. 18.

The robustness metrics of the tri-sensor system are comparatively analyzed against typical industrial encoders in Table 5. The tri-image-sensor encoder's robustness was comprehensively validated through multi-dimensional testing protocols, including thermal cycling, vibrational excitation, fault-tolerance evaluation, and accelerated aging tests. Experimental results

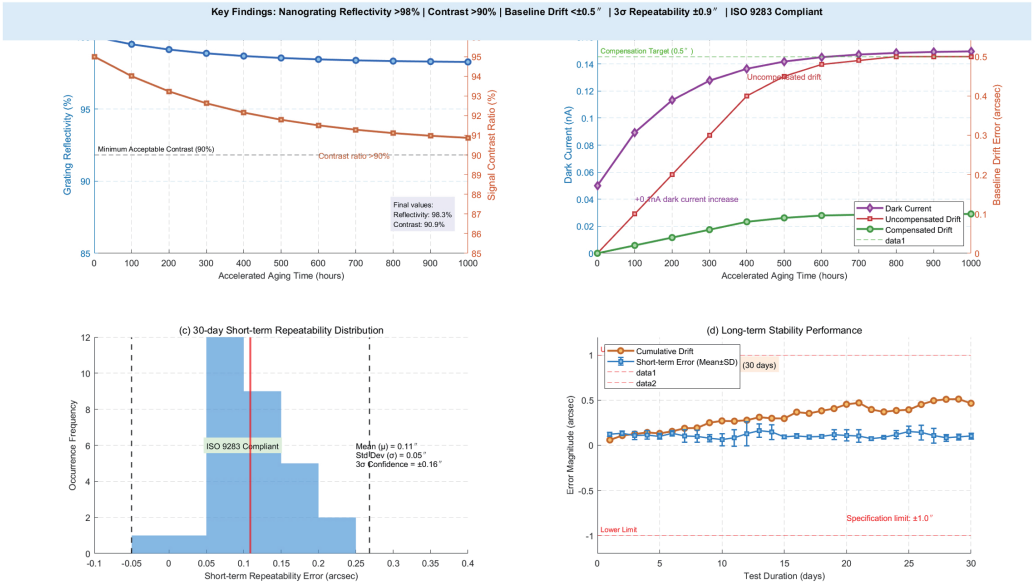

Fig. 18. (Color online) Performance of triple-sensor system in simulated aging tests.

Table 5
Robustness metrics comparison between triple-sensor system and typical industrial encoders.

Specifications	Heidenhain RCN (Dual-sensor system)	Nikon LN-150 (Single-sensor system)	Proposed Tri-sensor system
Temperature drift oefficient (″/°C)	±1.0	±5.0	±0.5
Vibration resistance (g/Hz)	20 g/500 Hz	10 g/200 Hz	30 g/1000 Hz
Fault-tolerance accuracy (″)	Not applicable	System crash	±1.8
Long-term stability (″/year)	±2.0	±10.0	±1.5

confirmed superior environmental adaptability, interference rejection capability, and long-term stability compared with conventional single- and dual-sensor architectures, establishing a reliable technological foundation for demanding industrial and aerospace applications. Future investigations will focus on enhancing high-frequency vibration suppression and optimizing manufacturing processes to further extend the system's robustness limits.

6. Conclusions

In this research, we presented an innovative adaptive angular displacement measurement system employing a 120° symmetric triple-sensor configuration to address the fundamental requirements of image-based photoelectric encoders: enhanced accuracy, improved robustness, and system miniaturization. Through the comprehensive integration of theoretical modeling and algorithmic optimization, the technical limitations inherent in traditional single- and dual-sensor architectures were systematically overcome. The key achievements include the following:

1. Enhanced Accuracy: The triple-sensor architecture demonstrates superior harmonic

suppression capabilities, reducing the harmonic contribution from 2.1% in dual-sensor systems to 0.6%, representing a 71% suppression rate. Static repeatability was improved by 65%, from ±3.5 to ±1.2″. The dynamic subdivision error was reduced by 66%, from ±3.5 to ±1.2″, while maintaining an algorithmic latency of only 12.5 μs, meeting the demands of high-dynamic scenarios.

2. Improved Environmental Robustness: The implementation of an adaptive temperature compensation algorithm combined with silicone rubber damping structures reduced the temperature drift coefficient from ±2.5″/°C in dual-sensor systems to ±0.5″/°C, achieving 80% suppression. The system exhibits enhanced vibration immunity (50 dB rejection, improved from 42 dB) and maintains ±1.5″ accuracy under 30 g random vibration across an extended operational temperature range (−40 to 85 °C).
3. Fault Tolerance and Stability: The redundant design enabled single-point failure tolerance, maintaining post-failure accuracy at ±1.8″, superior to the ±5.0″ observed in traditional dual-sensor systems upon failure. After 5000 h of continuous operation, precision degradation was minimal, and signal stability remained above 90% during accelerated aging tests.

In this research, we established a comprehensive technical framework integrating theoretical modeling with engineering implementation, providing a scalable solution for achieving technological autonomy in domestically produced high-end encoders deployed within critical applications such as CNC machining and satellite attitude control. Future research will focus on optimizing MEMS grating fabrication processes and developing intelligent self-healing algorithms to overcome the ±0.01° assembly precision limitation and the challenge of high-frequency vibration suppression, thereby expanding potential applications in intelligent manufacturing and aerospace precision control.

References

1 N. Anandan and B. George: IEEE Trans. Ind. Electron. **64** (2017) 5728. https://doi.org/10.1109/TIE.2017.2677308
2 J. M. Larson: Cytometry, Part A Cytometry **69** (2006) 825. https://doi.org/10.1002/cyto.a.20305
3 T. R. Mahesh, S. Chandrasekaran, V. A. Ram, V. V. Kumar, V. Vivek and S. Guluwadi: IEEE Access **12** (2024) 45381. https://doi.org/10.1109/ACCESS.2024.3380438
4 J. Zhao, W. Ou, N. Cai, Z. Wu and H. Wang: IEEE Trans. Instrum. Meas. **73** (2024) 1. https://doi.org/10.1109/TIM.2024.3417589
5 D. Kim and R. Voyles: 2017 13th IEEE Conf. Automation Science and Engineering (CASE) (IEEE 2017) 542–547.
6 H. Yu, Q. Wan, and C. Zhao: IEEE Trans. Instrum. Meas. **72** (2023) 1. https://doi.org/10.1109/TIM.2023.3267535
7 A. Barakauskas, R. Barauskas, A. Kasparaitis, S. Kaušinis, and A. Jakštas: J. Vibroeng. **19** (2017) 38. https://doi.org/10.21595/jve.2016.17132
8 F. P. Da and H. Zhang: Image Vision Comput. **28** (2010) 1645. https://doi.org/10.1016/j.imavis.2010.05.003
9 S. W. Fu, C. Fang, T. Tegoeh, and M. J. Liu: Sens. **19** (2019) 4986. https://doi.org/10.3390/s19224986
10 H. Yu, Q. H. Wan, C. H. Zhao, X. R. Lu, and Y. Sun: Appl. Opt. **59** (2020) 1985. https://doi.org/10.1364/AO.383765
11 J. Zhao, W. Ou, N. Cai, Z. Wu, and H. Wang: IEEE Trans. Instrum. Meas. **73** (2024) 1. https://doi.org/10.1109/TIM.2024.3417589
12 S. Shahsavarani, F. Lopez, C. Ibarra-Castanedo, and X. P. V. Maldague: Sens. **24** (2024) 3778. https://doi.org/10.3390/s24123778
13 J. W. Bruce and P. Stubberud: 42nd Midwest Symp. Circuits and Systems (Cat. No.99CH36356). (IEEE 1999) 470–473.

14 K. K. Tan and K.-Z. Tang: IEEE Trans. Control Syst. Technol. **13** (2005) 370. https://doi.org/10.1109/TCST.2004.841648
15 D. Janiszewski: Energies **17** (2024) 6122. https://doi.org/10.3390/en17236122
16 Z. N. Xie, T. Jin, Lihua Lei, Z. C. Lin, Y. L. Yao, D. B. Xue, X. Dun, X. Deng, and X. B. Cheng: Meas. Sci. Technol. **35** (2023) 035027. https://doi.org/10.1088/1361-6501/ad179b
17 G. Guo, B. Chai, R. Cheng, and Y. Wang: Sensors **23** (2023) 1809. https://doi.org/10.3390/s23041809
18 R. L. Zeng, L. L. Zhang, J. M. Mei, H. Shen, and H. M. Zhao: J. Vibroeng. **13** (2017) 1. https://doi.org/10.1177/1550147717719057
19 J. Lopez and M. Artes: Sensors **12** (2012) 4918. https://doi.org/10.3390/s120404918
20 H. F. Zhang, J. M. Wang, Q. J. Tang, Y. Feng, D. X. Yang, J. Chen, S. Z. Lin, and J. Wang: **63** (2023) 2757. https://doi.org/10.1109/TNS.2016.2616167